

Supporting Information for

“Origin of Giant Ionic Currents in Carbon Nanotube Channels”

Pei Pang, Jin He, Jae Hyun Park, Predrag S. Krstić and Stuart Lindsay

1. Experimental details	page S2
2. Ionic conductance distribution for devices with a floating gate ..	page S3
3. Dependence of the hysteresis in $G_{\text{ionic}}-V_g$ on sweep rate and raw data of Figure 2c	page S4
4. Measurements of gate leakage	page S5
5. Leakage current	page S5-S7
5.1 Leakage and gating.....	page S5
5.2 Large Cations ($\text{Ru}(\text{bipy})_3\text{Cl}_2$ electrolyte).....	page S6-7
6. Summary of gating efficiency for all devices	page S7-S9
7. Theory details	page S9-S38
7.1 Formulation of the approach.....	page S9-S12
7.2 Numerical Methods	page S12-S13
7.3 Choice of CNT charge, scaling currents and lengths	page S13-S18
7.4 Comparison with experiments	page S18-S19
7.5 Gating efficiency.....	page S19-S20
7.6 Analysis of the simulation results.....	page S20-S31
7.7 Slip length of a charged SWCNT.....	page S31-S34
7.8 Velocities and mobilities	page S34-S38
8. References	page S38-S40

1. Experimental details

1.1. CNT growth

We have used two kinds of catalysts for CNT growth by chemical vapor deposition (CVD): diblock copolymer-templated cobalt nanoparticles and ferritin-based iron nanoparticles. The diblock copolymer method has been described in detail in our previous publication.¹ A typical atomic force microscopy (AFM) image of an as-grown CNT and the diameter distribution is shown in Figure S1a and b. Iron loaded ferritin catalysts were produced following the procedure by Li et al.² with a theoretical loading of ~1200 Fe(III)/ferritin. After depositing ferritins onto SiO₂ or Si₃N₄ substrates, the substrate was heated to 800 °C in air for about 10 minutes to form iron oxide nanoparticles with an average diameter of 3.0 ± 0.9 nm as determined by AFM. CNTs were grown using ice-cold ethanol as the carbon source in Argon (138 sccm) and hydrogen (18 sccm) flow at 900-1000 °C for about 25-50 minutes. After the growth, the CVD system was cooled down to room temperature at the same gas flow rate. The diameter distribution measured by AFM is shown in Figure S1c. The CNTs grown by this method are not as reproducible as the cobalt catalyst method. However, we always got a large fraction of CNTs showing high electrical conductivity, which is attributed to large diameter SWCNTs and few-layer MWCNTs.

1.2. Solution preparation

10x Phosphate-Buffered (PB) stock solution with pH=7.4 was prepared beforehand. Immediately before use, the 10x PB stock solution was used to prepare 1M KCl with 10mM PB solution. The buffered 1M KCl solution was diluted with DI water to the final desired concentrations. The pH of the buffered KCl solution was adjusted by adding HCl and KOH. The concentration of the KCl solution is not affected by the pH adjustment at high concentration but will be affected at low concentration. For example, the chloride ion concentration is roughly 2mM instead of 1mM in 1mM KCl at pH 3 due to the addition of HCl solution. The salt solution was filtered and degassed by Ar for 10 minutes before use.

2. Ionic conductance distribution for devices with a floating gate

The ionic conductance distribution of all the working devices at 1mM KCl solution with floating gate is shown in Figure S1e. These devices display higher conductances than the devices we built with PMMA barriers on the SWCNTs.¹ This may be due to the new device geometry differences in the charge density in the barrier region.

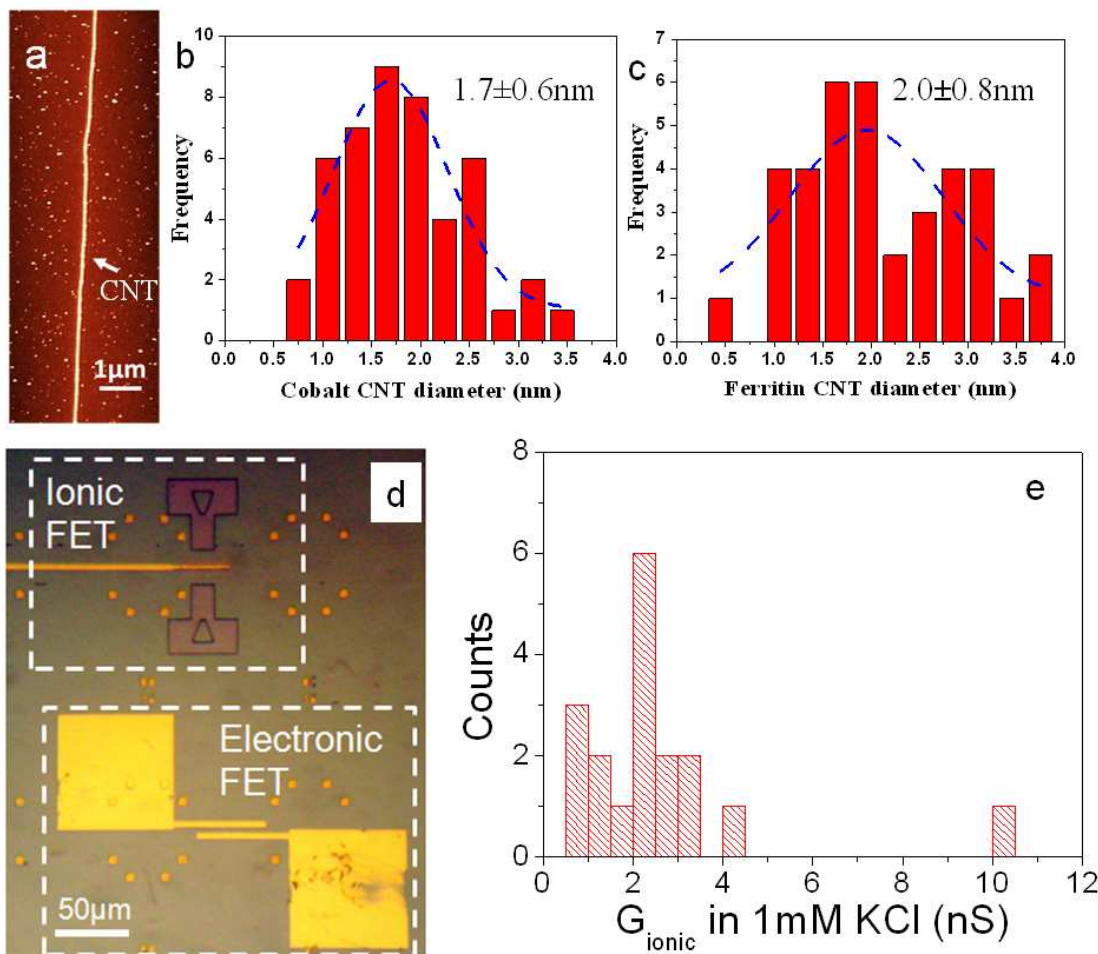


Figure S1. (a) AFM image of a CNT on SiO₂/Si substrate after growth. The height of the CNT measured by AFM was used to determine the diameter of the CNT. (b) A typical diameter distribution of CNT by cobalt method. A Gaussian fit gives the mean diameter 1.7 ± 0.6 nm. (c) A typical diameter distribution of CNT by Ferritin method. A Gaussian fit gives a mean diameter of 2.0 ± 0.8 nm. (d) Optical microscope image of a device showing both ionic CNT FET and electronic CNT FET. Both FETs were fabricated on the same CNT, guided by the metal markers. The electronic FET is gated using the Si substrate as a backgate. (e) Conductance distribution of all the working devices.

3. Dependence of the hysteresis in $G_{\text{ionic}}-V_g$ on sweep rate and raw data of Figure 2C

We found the hysteresis of G_{ionic} vs. V_g curves decreases with increasing sweep rate, indicative of a slow polarization process in the gate region. The gating efficiency was also reduced slightly with increasing sweep rate. We used a sweep rate at 60-80 mV/s for all measurements reported here. The corresponding I_g vs. V_g curves are shown in Figure S2b. The hysteresis increased with sweep rate, suggesting the capacitive current origin of I_g .

The raw data of Figure 2c, $I_{\text{ionic}}-V_g$ curves at different V_{ionic} and $I_{\text{ionic}}-V_{\text{ionic}}$ curves at different V_g , are shown in Figure S2c,d. The $I_{\text{ionic}}-V_{\text{ionic}}$ curves are almost symmetric at negative gate voltage and become more asymmetric at positive gate voltage. For example, at $V_g = -0.4\text{V}$, $|I_+/I_-|_{V_{\text{ionic}}=0.6} = 1.1$ and at $V_g = +0.4\text{V}$, $|I_+/I_-|_{V_{\text{ionic}}=0.6} = 1.4$.

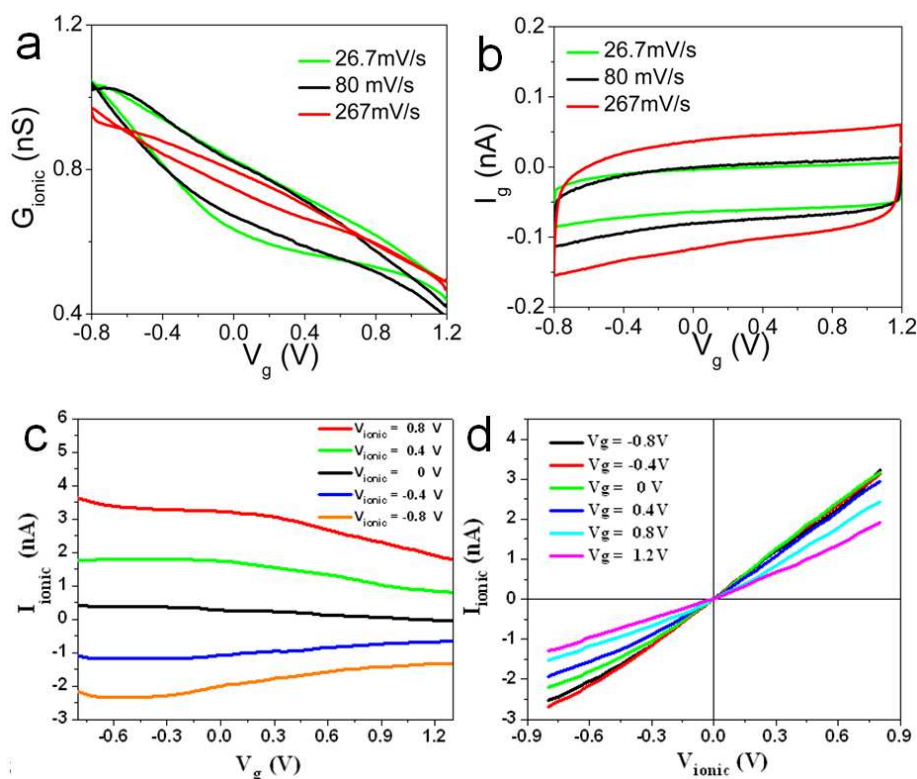


Figure S2. (a) G_{ionic} vs. V_g curves of one device at different sweep rates. The salt concentration is 1mM. (b) The I_g vs. V_g curves measured at the same time. (c) The I_{ionic} vs. V_g curves at different V_{ionic} . (d) The I_{ionic} vs. V_{ionic} at different V_g .

4. Measurements of gate leakage

Before the opening of the SWCNT, the gate current I_g in the applied V_g range appears to be purely capacitive (see Figure S3c). After the opening the CNTs with an oxygen plasma, I_g often shows a potential dependent current (i.e., sigmoidal shape for some cases) superposed on the capacitive charging current as illustrated by the blue curve in Figure S3d and Figure S4. Such change is likely due to some Faradic current leaking through the thin dielectric layer. The change in the I_g - V_g curves is utilized to signal the filling of solution inside the CNT.

5. Leakage current

5.1. Leakage current is not gatable

We have rigorously investigated the leakage current of our devices using KCl solution.¹ Control devices (no SWCNT) were build on the same chip as the devices containing CNTs and processed in exactly the same way. No current was measured when there was no CNT in the device (control device) and when the CNT was not opened by oxygen plasma. The ionic current was significantly reduced when the CNT ends were modified with bigger molecules. We have found the paths between plasma damaged PMMA resist surface and PDMS cover were the main leakage pathways. The device used for this paper has a 20-30 μm wide barrier, which is about 10 times wider than the previous devices. The leakage current from these new devices is always negligible (according to the results of corresponding control devices) when using the same oxygen plasma etching time (<30 sec, 600 mtorr, 7.3W) as the working devices. Ionic current was often observed after longer time etching (>40 sec). However, no gating effect was observed on these devices as shown in Figure S3c. We also monitored I_g (a pure capacitive current - blue curve in Figure S3c). From the I_{ionic} - V_g and I_g - V_g curves, we are able to judge if the ionic current is from the ionic flow through the interior of the CNT. We also found that there were a small fraction of CNT devices for which no ionic current was obtained after the normal 20-30 second oxygen plasma etching, despite the fact that SEM images showed that the CNT ends were opened. For these devices, the ionic current appeared after further plasma etching. In these cases we got similar results as were obtained in control devices (Figure S4) when sweeping V_g on the gate electrodes. Thus, we attributed the ionic

current to leakage current. These experiments show that only the ionic current through the interior of CNT is gateable.

5.2. Experiment of Ru(bipy)₃Cl₂

We measured ionic conductance using an electrolyte with a large cation, Ru(bipy)₃Cl₂. As shown in Figure S3b, the measured ionic conductance using Ru(bipy)₃Cl₂ through the device is about 10 times smaller (at V_g=0) than when using the same concentration of a KCl solution. A reduced Ru(bipy)₃Cl₂ flux (30% of the KCl) was also observed in MWCNT membrane (~7nm inner diameter).³ However, the measured conductance of Ru(bipy)₃Cl₂ is still much bigger (~3-4 orders of magnitude higher) than the calculated results based on a model of pure electrophoresis. In addition, the ionic current of Ru(bipy)₃Cl₂ through a non-damaged SWCNT device is gateable, as shown in Figure S3d. Interestingly, we obtained n type ionic transistor behavior (the transistor changed to p type when switching to KCl electrolyte). This suggests that the movement of bigger Ru(bipy)₃²⁺ cation was hindered even at negative gate voltage. The anion Cl⁻ became the major carrier at positive gate voltage (the positive gate voltage will attract the Cl⁻ to get into the CNT, overcoming the repulsion from the negative charged carboxyl groups at CNT ends).

The bulk diffusion constants of K⁺, Cl⁻ and Ru(bipy)₃²⁺ are 1.96×10⁻⁵, 2.00×10⁻⁵ and 0.52×10⁻⁵ cm²/s, respectively. If the contribution of current is mainly from diffusion and electrophoresis, the conductance of the same concentration KCl and Ru(bipy)₃Cl₂ solution should be similar (note the Cl⁻ concentration in Ru(bipy)₃Cl₂ is twice the value of Cl⁻ in KCl).

We also fabricated control devices with various leakage pathways by deliberately damaging the devices. For a control device with big leakage pathway, made by a mechanical scratch on PMMA surface or by using longer times and higher intensities of oxygen plasma treatment, the measured conductance of KCl and Ru(bipy)₃Cl₂ are similar. However, ionic conductance of Ru(bipy)₃Cl₂ obviously suppressed for device with 40-90 sec oxygen plasma treatment (Figure S3a). The decrease in ionic current is similar to the working device. The small PMMA pathways may also hinder the movement of bigger cations. Thus, an ion size dependence of the current is not necessarily a signature of

transport through SWCNTs. However, no gatable current was observed in all the devices that were made to leak via deliberate damage (Figure S3c). Thus the degree of gatability is a conclusive test of transport via the SWCNT.

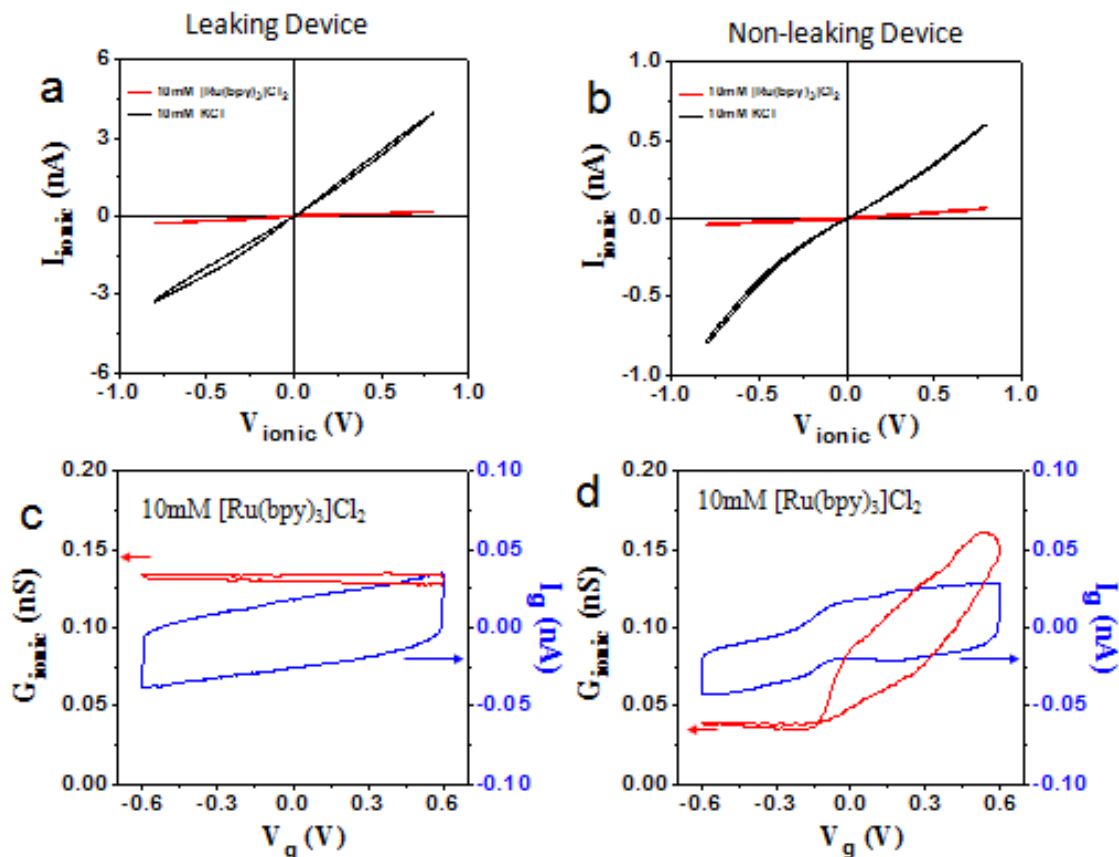


Figure S3. The $I_{\text{ionic}}-V_{\text{ionic}}$ curves of both a leaking (deliberately damaged) device (a) and working (non-leaking, non-damaged) device (b) for both 10mM KCl (black curve) and $\text{Ru}(\text{bipy})_3\text{Cl}_2$ (red curve) electrolytes. The $G_{\text{ionic}}-V_g$ (red curve) and I_g-V_g (blue) curves of both the leaking device (c) and the non-leaking device (d).

6. Summary of gating efficiency for all devices

Table S1 lists the ionic gating efficiency of all the working devices, measured at a V_g sweep rate of 60-80mV/s in 1mM buffered KCl solution, pH=7.4. In order to reveal the relationship between the electrical properties of the CNT and the gating efficiency, we measured the electrical transport properties of several devices, as color coded in table S1. The results of three devices, representing semiconducting, metallic and small band gap semiconducting CNT devices, are shown in Figure S4. The ambipolar behavior in the

electronic transport characteristic suggests small band gap SWCNT (outside diameters are estimated to be 3-5nm).⁴ The ionic gating efficiency of this device is about 0.1.

Table S1. Gating efficiency of all the measured devices in 1mM buffered KCl ,pH=7

Device Name	Gating efficiency ($\Delta G/G_+$)	Device Name	Gating efficiency ($\Delta G/G_+$)	Device Name	Gating efficiency ($\Delta G/G_+$)
S032L5L6	0.23	S058R8	1.01	SN00116R12	0.25
S028L9	0.58	S065L13	0.65	SN009R4	0.55
S028L5L6	0.46	S065L14	1.46	PF01L11*	0.007
S054R11	0.68	S110L7	0.47	PF01L14*	0.151
S054R9R12	0.95	S110L1	5.24	HF5L7*	0.10
S054L8L11	0.88	SN009R12	0.7	PF03L11*	1.62
S058R11	0.22	S204L13	0.83	PF03R2*	3.76
				PF03L4*	4.85

Note: 1. Red = metallic CNTs, blue = semiconducting CNTs, orange = small gap semiconducting CNT.
2. * CNTs grown using the ferritin method.

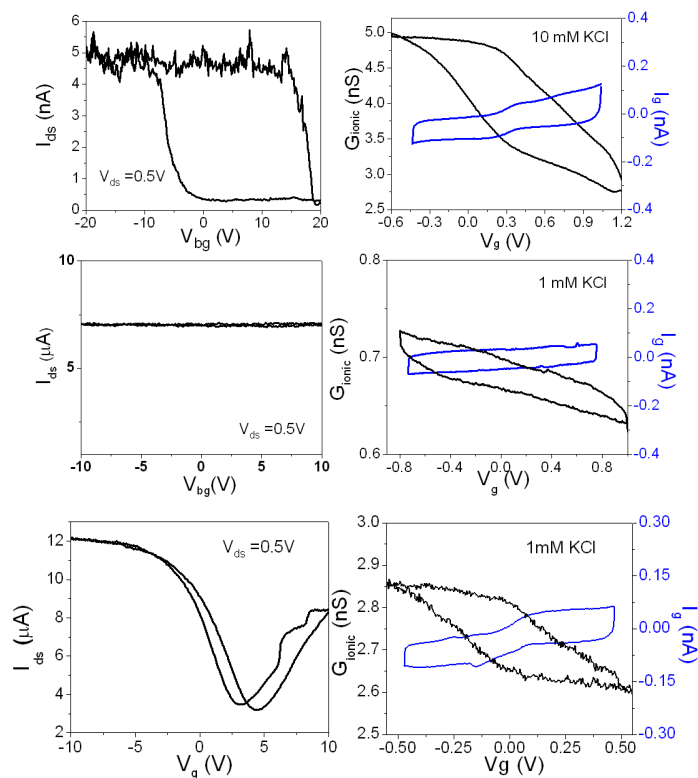


Figure S4. The electrical transport characteristics (left column) and ionic transport characteristics (right column) of device SN009R12 (upper row), PF01L14 (middle row), and HF5L7 (lower row). The CNT in Device HF5L7 was grown by ferritin method. The CNT length is about 20 μm .

7. Theory details

7.1 Formulation of the approach

We base our study of the present micro-nano-fluidic⁵ system on the continuum hypothesis. Having in mind that a typical mean free path in water is $\lambda \sim 3 \text{ \AA}$ and using the diameter of CNT as a characteristic system length ($d = 2 \text{ nm}$), the Knudsen number $\lambda/d \sim 0.1$ is still small enough so that the continuum approximation is valid. In addition, the Reynolds number for the liquid in normal conditions is here very small, guaranteeing laminar motion in all cases considered. However, having in mind that in the range of KCl concentrations (1 mM – 1 M) the Debye length varies from 3 -100 \AA , a caution is needed at the higher end of electrolyte concentrations (1 M), due to the problems the continuum fluid dynamics might have in the double layer to the internal CNT surface as the dimensions of the double layer approach the molecular scale.

To find the steady state fluid flow we numerically solve a set of time-independent coupled partial differential equations, the Poisson-Nernst-Planck-Stokes (PNPS) equations.⁶⁻⁸ The Poisson equation defines electrostatic scalar potential ϕ as response to the local excess electric charge, $\rho_e = (c_+ - c_-)F$ in the environment of relative dielectric constant ϵ_r , where c_{\pm} are the instantaneous volume densities of the positive (+) and negative (-) ions, and F is the Faraday constant.

$$\nabla \cdot (\epsilon_r \nabla \phi) = -\frac{\rho_e}{\epsilon_0}, \quad \rho_e = (c_+ - c_-)F \quad (\text{S1})$$

This equation in its integral version describes the total electric field flux through a surface enclosing an excess charge. The Nernst-Planck equation, in its integral form, defines the conservation of the flux, $\vec{\Gamma}_{\pm}$, of charged particles (of charge $z_{\pm}e$, where e is an elementary charge) through an arbitrary closed surface, i.e. the conservation of the total electric current, and contains electrophoretic (proportional to the ion mobility $\mu_{m,\pm}$), diffusive (diffusion constant D_{\pm}) and electroosmotic terms (proportional to the velocity of the fluid element \vec{u}), and its local form is

$$\nabla \cdot \vec{\Gamma}_{\pm} = \nabla \cdot (-D_{\pm} \nabla c_{\pm} + z_{\pm} \mu_{m,\pm} F c_{\pm} \nabla \phi + c_{\pm} \vec{u}) = 0 \quad (\text{S2})$$

Finally, the Stokes equation is the approximation of Navier-Stokes equations with a negligible inertia term,

$$-\nabla p + \eta \nabla^2 \vec{u} = -\rho_e \nabla \phi \quad (\text{S3})$$

and yields the fluid velocities, which depend on the electric potentials, charges, external pressure gradients ∇p and the fluid viscosity η through the assumption of the full hydration of charged particles. Thus, the fluid moves with the charged particles. The conservation of the mass flux, i.e. zero total flux of the fluid exiting any closed surface, compatible with the assumption of the fluid non-compressibility, adds the equation

$$\nabla \cdot \vec{u} = 0 \quad (\text{S4})$$

We use an idealized azimuthally symmetric system geometry in simulations, which is schematically shown in Figure S5.

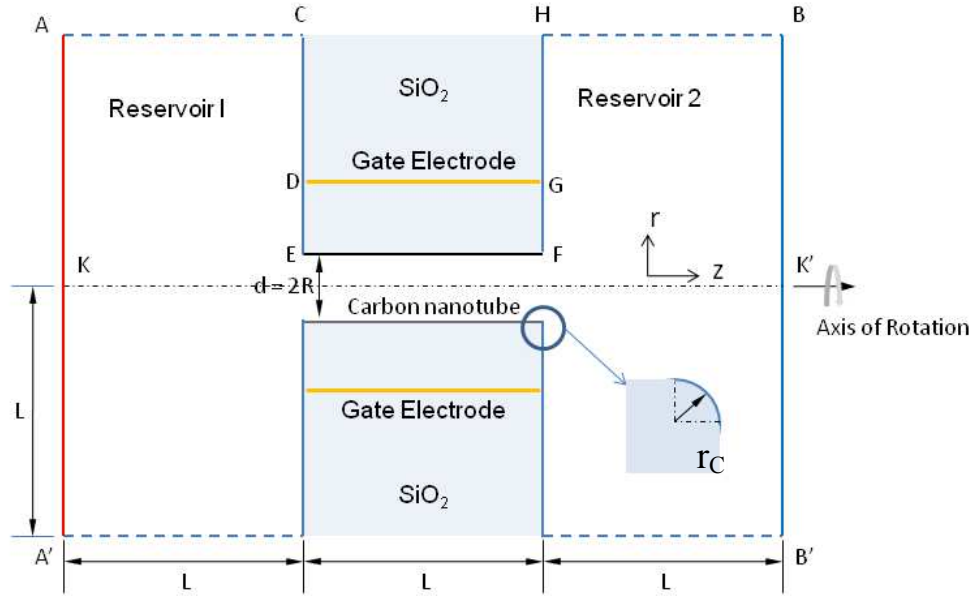


Figure S5. Geometry of the idealized axially-symmetric system

The cylindrical gate electrode has a radius of 20 nm, and is chosen to be the same length, L , as the CNT. It is embedded in the SiO_2 dielectric ($\epsilon_r=3.9$). It encloses the carbon nanotube surface of radius $R=1$ nm, also embedded in SiO_2 . This is an approximation to the real gate geometry (Figure 1 in the main text) which is not axially

symmetric. The reservoirs (inlet 1 and outlet 2) and the CNT are filled with an aqueous solution ($\epsilon_r=80$) of potassium- chloride (KCl) of concentration c . The reservoir dimensions, L , in both axial and radial directions, are chosen to be the same as the CNT length (L).

The physics of the system is governed by the boundary conditions, applied to the charge concentrations $c_{\pm}(r,z)$, potentials $\phi(r,z)$ and velocities $\vec{u}(r,z)$, where r and z are radial and axial coordinates (Figure S5). The source-drain voltage, V_0 , is set between the electrodes AA' and BB' (by the Dirichlet type boundary conditions) with the potentials at the electrodes, $\phi_{AA'} = +V_0/2$ and $\phi_{BB'} = -V_0/2$. The potential of the gate electrode, V_g , is varied. The electrolyte concentration c of KCl is set in the infinitesimal layers AA' and BB' of the reservoir electrolyte, adjacent to the electrodes. Fluxes of the charged particles as well as the fluid velocities in the direction of the normal to all solid surfaces facing the fluid are set to zero, i.e. $\vec{\Gamma}_{\pm} \cdot \vec{n}_w = 0$ and $\vec{u} \cdot \hat{n}_w = 0$. “Far-field” boundary conditions are $\frac{\partial \phi}{\partial r} = 0$, i.e. there is zero electric field entering the surface, and these are set at the far-side reservoir surfaces AC and HB. No-slip boundary conditions, the tangential component of velocity $u_r=0$, are set at the side reservoirs walls, i.e. at the surfaces CE and HF. The perfect-slip boundary conditions, i.e. $\partial u_z / \partial r = 0$, are set at the carbon nanotube walls (including the smoothed mouth regions).⁹ Analysis and justification of the choice of the perfect-slip boundary conditions is given in S 7.7.

The carbon nanotube is assumed to be an infinitely thin cylindrical surface between the fluid and solid (SiO_2) media, with a floating potential boundary condition, specified only by a total, predefined charge $-Q$ located at the tube. We stress that no surface charge-density distribution is pre-defined, allowing the system to self-adapt this quantity self-consistently with the solution of the PNPS equations. The charge $-Q$ can originate at the surface from the negative-charged carboxylate groups at oxygen plasma etched CNT ends and other charges (impurities, contaminations, defects) near or on the CNT,¹⁰ inducing excess positive volume charge in the tube in keeping the system electrically neutral. However, the charge $-Q$ can be induced at the CNT surface also by

the excess cation volume charge in the tube, emerging from the filtering of anions at the tube entrances by the negative-charged carboxylate groups at the entrances.

7.2 Numerical Methods

As detailed in S7.1, our simulations are based on the continuum approximation, assuming the micro-nano fluid system in a steady flow, with small Knudsen and Reynolds numbers, incompressible Newtonian fluid with the usual conservation laws of mass, energy, momentum. This is described by the set of the time-independent partial differential equations which we solve numerically, self consistently, seeking fulfillment of all conservation laws with high accuracy (3-4 significant digits), and full convergence at a fine finite elements numerical mesh, using the multiphysics and modeling software package COMSOL.¹¹ At each iteration, a sparse matrix form is constructed from the finite element discretization of equations (S1-S4). The algorithm employed (MULTifrontal Massively Parallel sparse direct Solver, MUMPS¹²) repeats the damping-factor reduction until the relative error is less than in the previous iteration or until the damping factor underflows its predefined minimum. The relative tolerance in all present calculations was set to be below 10^{-6} .

The main problem in the numerical simulation of the fluid dynamics defined by equations (S1-S4) for the system geometry shown in Figure S5 is a competition of the large and small quantities, caused by huge difference in the reservoir size and CNT length of characteristic dimension L and the CNT of diameter $d \ll L$. This geometry difference leads to large gradients in relevant physical quantities (charge densities, electrical potential) at the mouth regions of the CNT. These difficulties were somewhat relaxed by smoothing the corners in the mouth region of the CNT by a curvature of radius r_C , as shown in the inset of Figure S5. A fine numerical mesh was required, especially near the nanotube walls, electrode surfaces and other boundary surfaces as well as in the tube entrance regions, as shown in Figure S6a.

Refinement of the mesh was done iteratively until the total electric current in inlet and exit reservoirs and in the tube was found to be identical to within three digits, a goal that was difficult to achieve numerically. Typically, the size of an axial numerical grid element was smaller than 0.1 nm in the entrance-exit regions of nanotube, while the

minimum size of the numerical element in the radial direction in the interfacial region of the nanotube and electrolyte was less than 0.01 nm. The calculations showed the best stability with rectangular finite elements whose shape follows the geometry of the system for most of the computational domain. Exceptions are the mouth regions of the nanotube in which the diameter of tube was gradually changing, where we used triangular elements, as shown in Figure S6b. The number of elements was typically 170 in the axial direction and 90 in radial direction. The total number of numerical elements was 15,600, consisting of 15,100 rectangular elements and 500 triangular elements.

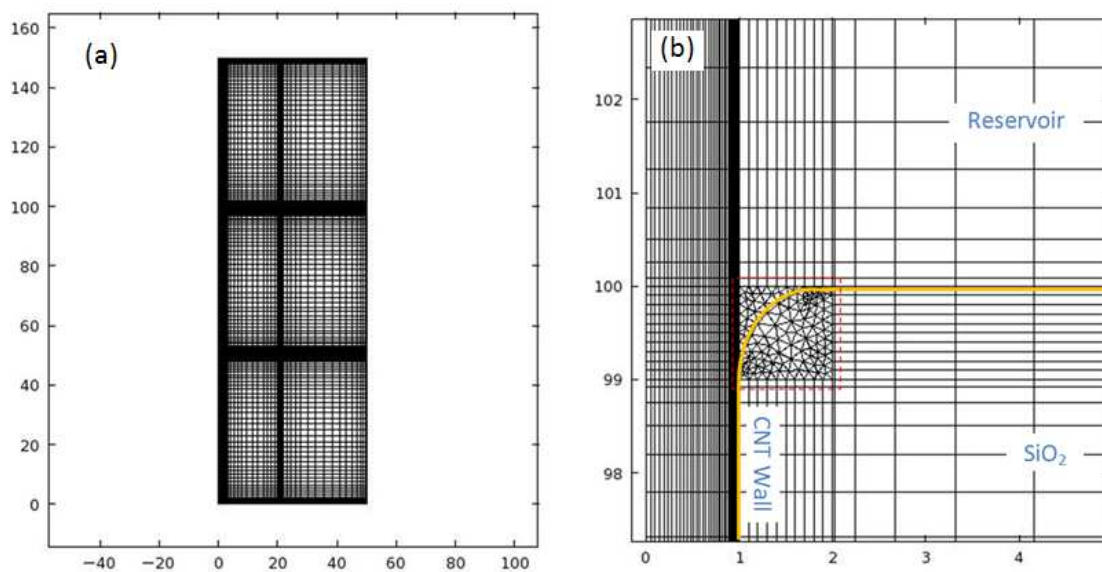


Figure S6. Typical grid system for computation. (a) Entire domain. The mesh density is high near nanotube walls, entrance regions, electrodes and other walls; (b) Enlarged mesh plot for the tube-mouth region. Yellow line indicates the solid-electrolyte boundary. The triangular meshes are used only for the region enclosed by the red dashed line.

7.3 Choice of CNT charge: Scaling currents and lengths

The computed ionic conductance depends strongly on the chosen CNT surface charge Q , as well as on the length of the tube. These effects are illustrated for calculations of the ionic conductance in Figure S7. This conductance is defined by $G = I_0 / V_0$, where I_0 is the total electric current, integrated over a cross section of fluid. We keep the tube diameter

$d=2$ nm constant when varying the tube length, L , and the reservoir dimensions. On varying the tube length we find that many measured features do not depend on the absolute values of total currents or the system conductance, as discussed and illustrated below.

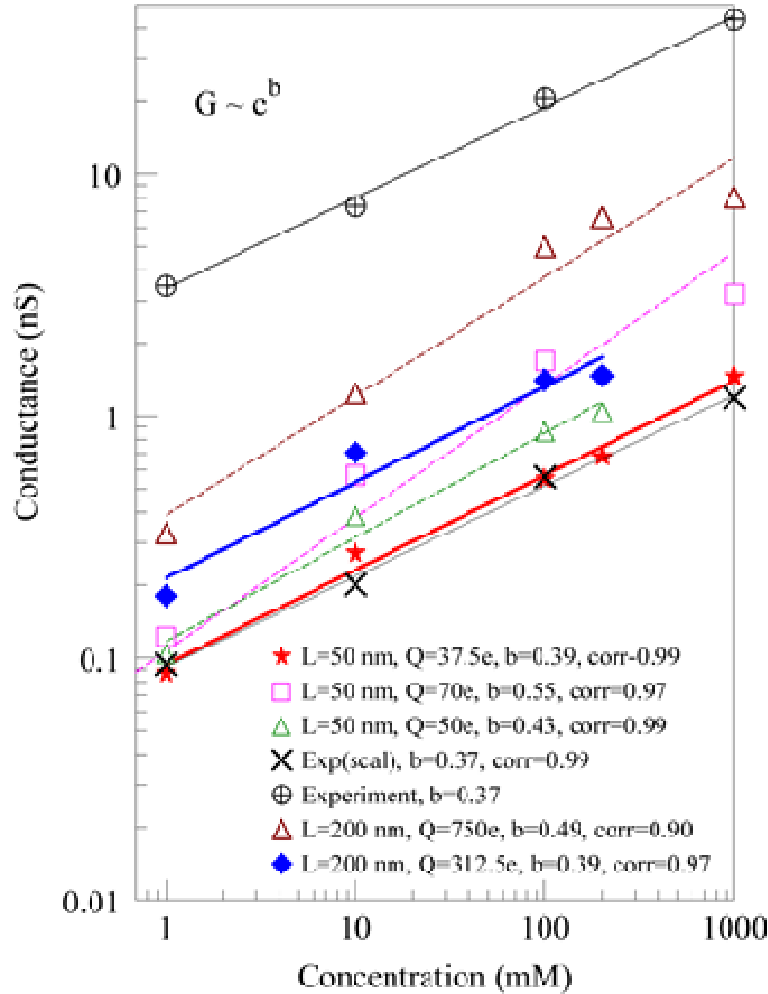


Figure S7. Ionic conductance vs. KCl concentration c obtained by experiment and simulations for various surface charges Q of the CNT and various tube lengths L . Q values in the legend are absolute values of the negative charges at the CNT surface, and corr are the correlation factors defining the quality of the power-law fitting ($\text{corr}=1$ is a perfect fit).

In case of $V_g=0$, our experimental measurement with both $L=20$ μm and $L=2$ μm SWCNT show almost perfect linear dependence in log-log scale of conductance G on electrolyte concentration c , having the slope of ~ 0.37 . Our calculations for various (much

shorter) lengths of 50 nm and 200 nm (Figure S7) also show approximately similar dependence of G on c , when varying the total surface charge Q at the CNT, where the slope and the quality of power fit depends on Q . Therefore, reasonable hypothesis for determination of Q is that the $G(c)$ is in the form of the power law, $G=A(L)c^b$, where possible length effect are contained in the prefactor $A(L)$, while the exponent b is independent on the tube length. Using this hypothesis, varying Q and solving PNPS equations, and fitting the slope of our computed results $G(c)$ to the experimental ones, trying to meet a similar exponent b as in the experiments, with the correlation factor close to 1, we obtain Q for various lengths. Thus, $Q=37.5e$ for $L=50$ nm (corr=0.99) and $Q=312.5e$ for $L=200$ nm (corr=0.97), in both cases $b=0.39$ (Figure S7). In these simulations $V_g=0$. The experimentally obtained value of $b=0.37$ fits the power law with corr=0.99.

From Figure S7 it is obvious that the ionic conductance is quite sensitive to the value of the total charge Q at the surface of the CNT. This is further illustrated at Figure S8. Thus, for scaled charges $q=|Q|L_0/L$ less than $q\sim 0.8\times 10^{-17}$ C (Q , the total charge on the floating CNT surface at $L=50$ nm, is assumed negative) the total ionic conductance is weakly dependent on κ . At larger q , the figure shows that the conductance tends to saturate with q , and the saturation level of conductance increases with the CNT length.

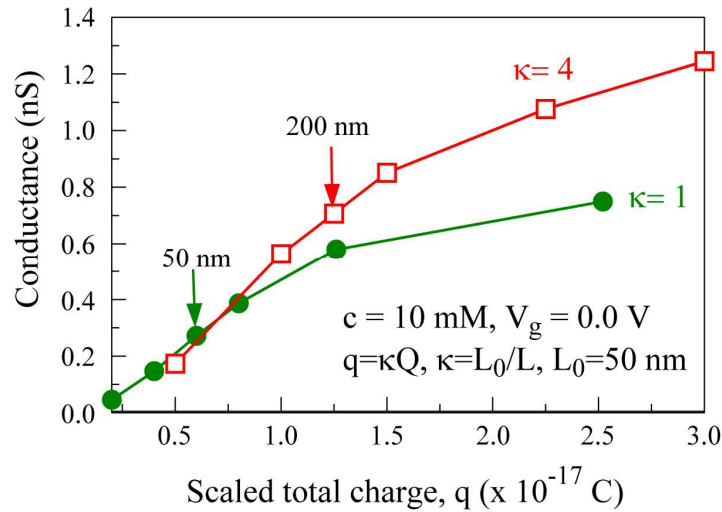


Figure S8. Ionic conductance vs. scaled total charge assumed at the CNT surface, for two different lengths of the CNT, $L=50$ nm (filled circles) and $L=200$ nm (hollow squares).

Given a total charge, Q , it is interesting to see how surface charge distributes along the tube surface as a response of the solution of the PNPS equations to the applied source-drain voltage and length L . A key issue is whether that surface distribution could be responsible for the higher “charge capacity” of the longer tubes.

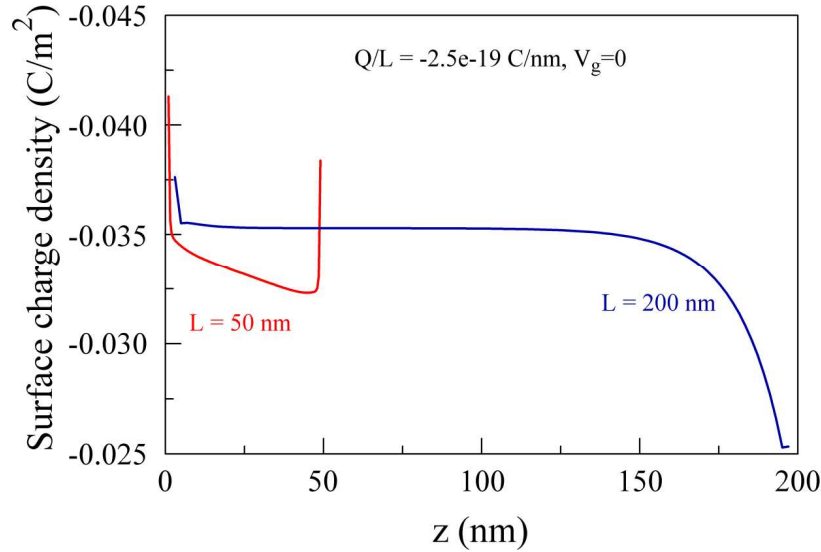


Figure S9. Axial distributions of the surface charge densities along the carbon nanotubes of different lengths for zero gate voltage.

In Figure S9 we show the axial distribution of the surface charge density for the two CNT lengths (at $V_g=0$) with the same total scaled charge QL_0/L at both tube surfaces. We stress that there is an expected jump in the surface charge density at the very ends of the tube, smoothed here by adding a curvature of radius of 1 nm (for $L=50$ nm) and 3 nm (for $L=200$ nm) to the ends of the tubes, as illustrated in Figure S5. It is not surprising that the negative charge of the tube is shifted toward the positively charged source electrode AA' (Figure S5), and the total variation of the charge density is mainly determined by the source-drain voltage. Obviously for $L=200$ nm the charge density can still “fill” the range between $z=0$ and $z=200$ nm, while for $L=50$ nm it almost linearly connects the charges at the two ends. By increasing the charge Q at the longer tube, the axial distribution of the surface charge density increasingly look like the one at $L=50$ nm, with appropriate increase of the total system conductance. We note that the source-drain

voltage V_0 is set to 1.25×10^{-2} V for $L=50$ nm and 5×10^{-2} V, in case of $L=200$ nm. If compared to the system with $L=20$ μm , with linear scaling of voltages these would correspond to the source-drain voltage of 5 V. Further decrease of the voltage for these small tube lengths results in a too low signal to numerical noise ratio in the simulations, but our simulations show that the current is still linear in voltage over this range, so that the conductance, $G=I/V$, is correctly calculated.

The numerical solution of the system of equations (S1-S4), done without further approximations, as well as the small-big geometry of the system require small dimensions of the model system (relatively to the experiment) in order to obtain the appropriate convergence and accuracy of the numerical procedures and validation of conservation laws (of mass, of electric current). We have chosen not to compromise the small diameter of the nanotube (here $d=2$ nm), but rather to reduce the axial length of the tube to $L=50$ nm, with appropriate adaptations of other system dimensions as in Figure S5, still keeping $d/L \ll 1$. According to the discussion above and comparisons with the measured relative quantities, this choice does influence the absolute value of the system conductance, but not the mechanisms of the physical phenomena in the system, which are a consequence of the small d/L values as well as of the special features of the CNTs.

After many simulations and comparison with the measurement, we choose $L=50$ nm, and $Q=-37.5e$ for the total surface charge at the tube. This yields the fit in Figure S8, for the gate potential $V_g=0$, in form

$$G = S c^{0.39} \text{ nS}, \quad (\text{S5})$$

where $S=44.34$ nS is the scaling factor needed for comparison with experimental results. Here c is the dimensionless concentration relative to 1 M-.

As seen in Figure S10, for a tube long enough, the total current over most of the tube length is by far dominated by the electroosmotic component, while a significant mixing of all three components of the current (electroosmotic, diffusion and electrophoretic) is present only close to the tube mouths. Some of the current components in this region can even be negative, i.e. flow in the direction opposite to electric field between source-drain electrodes. But obviously, the longer tubes support larger charges Q , resulting in almost proportionally larger electroosmotic currents.

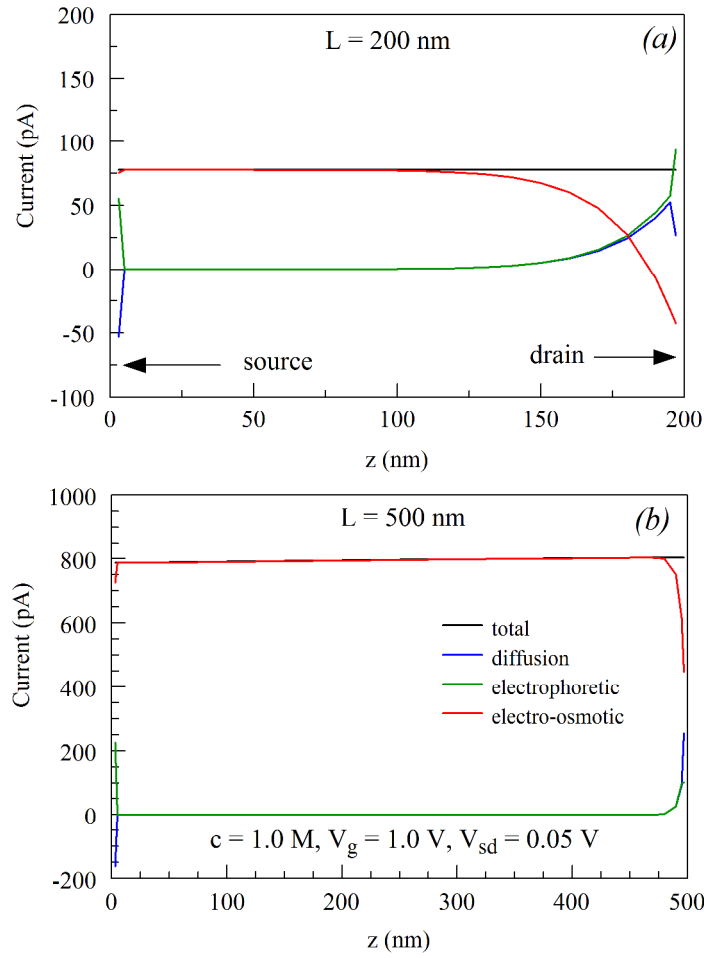


Figure S10. Components of electric current through the CNT for $V_0=1$ V, and $c=1$ M, $V_{sd}=0.05$ V, for the CNT lengths of (a) $L=200$ nm, $Q=-6 \times 10^{-17} C = -369e$, and (b) $L=500$ nm, $Q=-4 \times 10^{-16} C = -2500e$. The ratio of electroosmotic current (red line) to electrophoretic current is 234:1 for $L = 200$ nm and 3943:1 for $L = 500$ nm. The 3nm rounded ends of the tubes are not shown.

7.4 Comparison with experiments

Using the unique scaling in equation (S5) for $G(c)$ for $V_g=0$, we were able to reproduce by PNPS simulation the decreasing trends of measured ionic conductance with the gating voltage, V_g , for various KCl concentrations, as shown in Figure 3a of the main text.

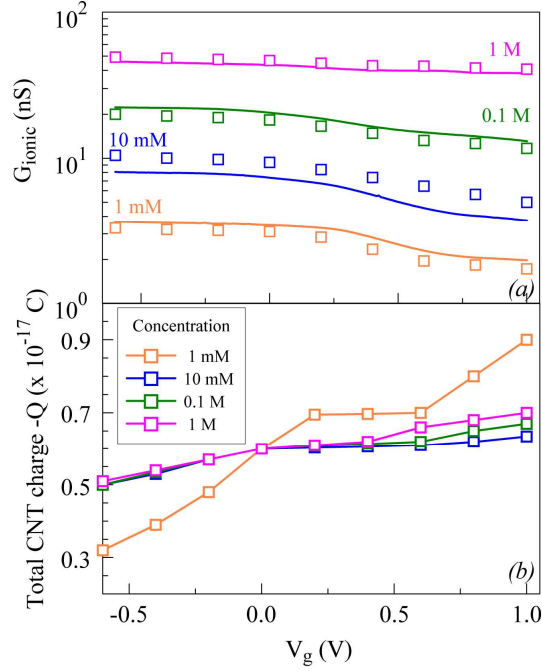


Figure S11. (a) Comparison of experimental results (solid lines) for ionic conductance with the simulated ones (symbols), for various concentrations of KCl, for $Q = -6 \times 10^{-18}$ C = $-37.5e$, using the common scaling form, equation (S5), for $V_g = 0$. For nonzero gate voltages the total charge was adapted as shown in (b).

As expected from the derivation of the scaling $G(c)$, (equation S5), in the S7.3, the agreement of the experiments and simulations is good around $V_g = 0$ (after one of the curves simulated was normalized at $V_g = 0$ to the absolute values of the measured conductance). When the gate voltage was changed from zero value, the agreement of measured and calculated $G(V_g)$ can be significantly improved from those at Figure 3a in the main text if we allow the charge on the tube, Q , to vary as a function of the gate bias (a reasonable consequence of polarization). Interestingly, the amount of ΔQ for almost perfect agreement along the range of V_g is very small, within 20%, and almost independent on c (Figure S11b). The exception is the lowest salt concentration (1mM) where the required variation was somewhat larger.

7.5 Gating efficiency

Table S2 shows values of E-field and excess charge for just one value of r at the middle of a 50 nm long tube to illustrate qualitatively the origin of the maximum in the measured

gating efficiency at $c = 10 \text{ mM}$. As discussed in S7.4, we here vary the charge Q with V_g to fit the experiment. The axial field (fourth column) rises very rapidly with increasing salt concentration since the electrophoretic voltage drop in the reservoirs is decreasing due to the increased conductance of the electrolyte. The electroosmotic flow through the CNT is proportional to the product of excess charge and the fluid velocity $u(z,r)$, and since $u(z)$ is proportional to axial electric field in the tube $E(z,r)$, we have approximately $\Delta G/G_+ = G_-/G_+ - 1 \approx (nE_-)/(nE_+) - 1$ (last column). We note that the radial change of the electric field and volume charge is slow enough to establish the approximate ratio without doing the formal integration over the cross-sectional area of the tube.

Salt concentration	V_g (V)	Excess charge $n(M)$	E-field E (V/m)	nE	$(nE_-)/(nE_+) - 1$
	-0.6	0.175	4152.0	726.2	0.732
1 mM	0.0	0.252	2975.9	749.9	
	1.0	0.276	1518.1	419.3	
	-0.6	0.329	8242.1	2713.3	1.542
10 mM	0.0	0.302	7938.0	2401.2	
	1.0	0.168	6357.7	1067.4	
	-0.6	0.401	15383.0	6170.1	0.661
0.1 M	0.0	0.376	15126.8	5681.6	
	1.0	0.268	13849.9	3714.5	

Table S2. Analysis of fields, charges and flow along $r = 0.9 \text{ nm}$ for a 50 nm long tube. Note that this selection of the tube volume results shows a volume charge that is not the same for each value of $V_g=0$ (but the integrated charge is, of course).

7.6 Analysis of the simulation results

Here, we illustrate the response of the charges, potentials and electric fields to the gate voltage. In most cases we show variations which correspond to the extreme and the mid values of V_g , i.e. -0.6V , 0 V and 1 V . Although the gate electrode is modeled as a cylinder around the CNT, end effects are too strong to keep the charge distribution homogeneous. Of course, the positive gate voltage induces larger negative charge in the middle of the tube while the negative V_g suppresses this charge from the mid of the tube. The slight asymmetry of the charge density at the center of the tube is caused by the

polarization by the source-drain voltage, making the distribution more negative toward the positive source. The positive excess volume charge in the tube, induced by the CNT surface charge follows similar polarization patterns, shown in Figure S12. These axial charge distributions are presented for $r=0.9$ nm, i.e. close to the CNT inner wall surface (at $r=1$ nm). The radial distributions of the volume excess charge for middle of the tube are presented in Figure S13. Although the Debye length for $c=10$ mM is close to $d_b=3$ nm, concentration of the excess charge in the tube is much higher, which yields smaller effective Debye lengths, for example $d_b=0.6$ nm for 0.25 M, which results in about a 40% average increase of the excess charge concentration over the radius (for $V_g=-0.6$ V). The variation with V_g decreases for smaller concentrations.

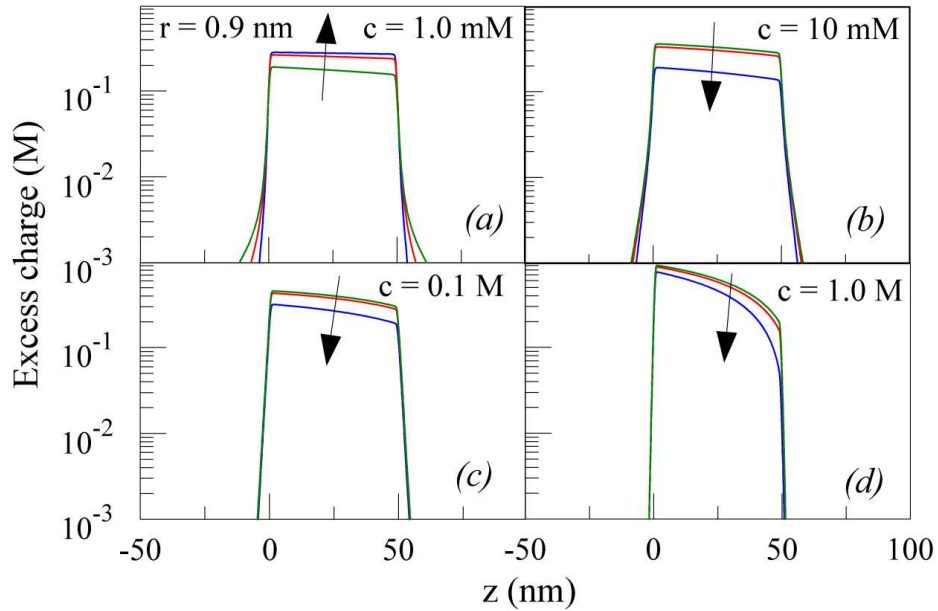


Figure S12. Axial distribution of the volume density of the excess charge from the source to the drain electrode, for the three values of the gate voltages, $V_g = -0.6, 0, 1$ V, at the radial distance of $r=0.9$ nm from the system axis. Concentration of KCl in the reservoirs was varied at (a), (b), (c) and (d) panels.

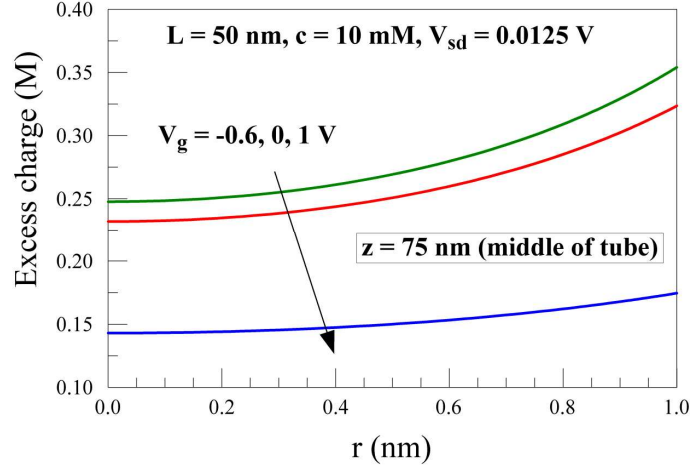


Figure S13. Radial distributions of the excess charge density at $z=75$ nm (middle of the tube), for the same conditions as in Figure S15 and one concentration ($c=10$ mM).

The excess charge in Figure S13 decreases with increase of the gate voltage V_g , in agreement with the decrease of the tube conductance with V_g . Also, with exception of 1 mM, the axial distributions of the positive volume excess charge density close to the tube wall in Figures S12 show trends consistent with the decrease of the current (Figure S11a). The full picture is not as simple. The correction of excess charge (Figure S11b) used to get agreement with the measured characteristics, shows an increase with V_g . However, the surface charge density in the middle of the CNT also increases with V_g , opposite to the volume behavior of the excess charge density inside the tube, though this trend reverses at the tube ends (Figure 3d in the main text). This is a consequence of the accumulation of excess charge in the reservoirs (Figure 3c in the main text). This interplay is illustrated by the change in the excess charge values at various locations as a function of gate voltage as listed in Table S3. We note that surface charge at the source and drain electrodes is negligibly small due to the small applied voltage (0.0125 V). Being of opposite sign at source and drain these contributions cancel out in any case, and are not shown in the charge balance of the Table S3. When $V_g=0$, the total charge at the CNT surface of $-37.5e$ is well balanced by the volume excess charge inside the tube ($\sim+26e$), the rest of charge at the source reservoir mouth ($\sim+6e$) and the drain reservoir ($\sim+4e$) as well as a small surface charge of $+1.25e$ at the gate surface well balance the CNT surface charge, making the system charge-neutral. However, this is not a case when a gate potential is applied, since the “charged” gate potential brings unbalanced surface

charge into the system. For the V_g as large as -0.6V or +1 V the total surface charge at the both sides of the (thin) gate electrode has a large negative or positive value (hundreds of electronic charges), and it is not fully balanced by the volume charges in the reservoirs and nanotube and surface charge at the CNT. In addition to the volume charge in the tube, which is consistently positive and decreasing with V_g , a large volume charge is induced at the reservoirs close to the CNT mouths. This induced charge of almost same size at both mouths of the CNT is positive for V_g negative, and negative for V_g positive. In both cases the charge at the entrances of the CNT at the reservoir sides is significantly larger than the total volume charge in the CNT (due to much smaller radius of the CNT than of the reservoirs).

	$V_g = -0.6 \text{ V}$	$V_g = 0.0 \text{ V}$	$V_g = 1.0 \text{ V}$
Total charge at CNT surface	-31.25	-37.5	-39.69
Excess volume charge in CNT	28.14	26.03	15.77
Source Reservoir	88.40	6.28	-131.36
Drain Reservoir	86.05	3.89	-133.92
Total in fluid: CNT+reservoirs	202.59	36.20	-249.51
Gate to CNT	-68.03	1.29	116.84
Gate to Far Field	-94.03	0.0023	156.86

Table S3. Distribution of the charges (in elementary charges e) through the system when varying the gate potential ($c=10 \text{ mM}$).

As seen in Figures S14 and S15, the huge values of the charge are a consequence of the large difference in size between the reservoir and the tube. Note that the average volume charge densities in the reservoirs in both radial and axial directions are much smaller than the average density in the tube (insets in Figures S14). It is interesting to note that there is a bump of the charge density in the radial distributions due to the vicinity of the charged gate. Also, as seen in the axial distributions, the excess charge is exactly decaying over the Debye length from the SiO_2 boundary (i.e. $\sim \exp(-z/D_b)$), reflecting the double layer formed between at the boundaries between fluid and the SiO_2 .

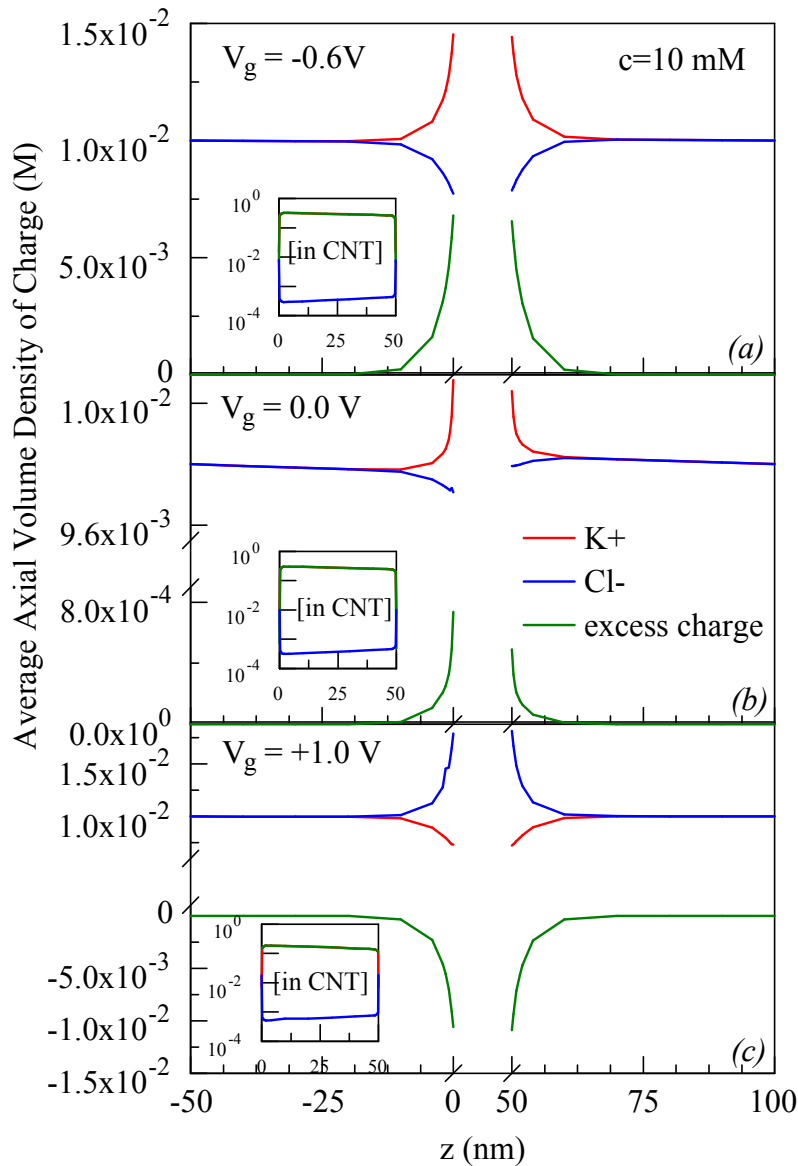


Figure S14. Axial distribution of charged particles and excess charge through the system, averaged over the cross sections of the reservoirs and tube

The accumulation of charges at the CNT mouths in the reservoirs contributes to the strong diffusion component peaks of the total current, balanced by the same but of opposite sign peaks of the electrophoretic currents, as illustrated in Figure S16, for the case of $V_g=0$. These peaks seem to maximize at about 100 mM KCl. Inside the tube the current is dominated by the electroosmotic current, though a sizable contribution of diffusion current is present. At 1M KCl, all three components of the total current make similar contributions for a tube of 50 nm length. However, such a strong dominance of all

three components for 1M is a consequence of the relatively short CNT length. As seen in Figure S10, for longer nanotubes the electroosmotic component dominates over the most of the tube length.

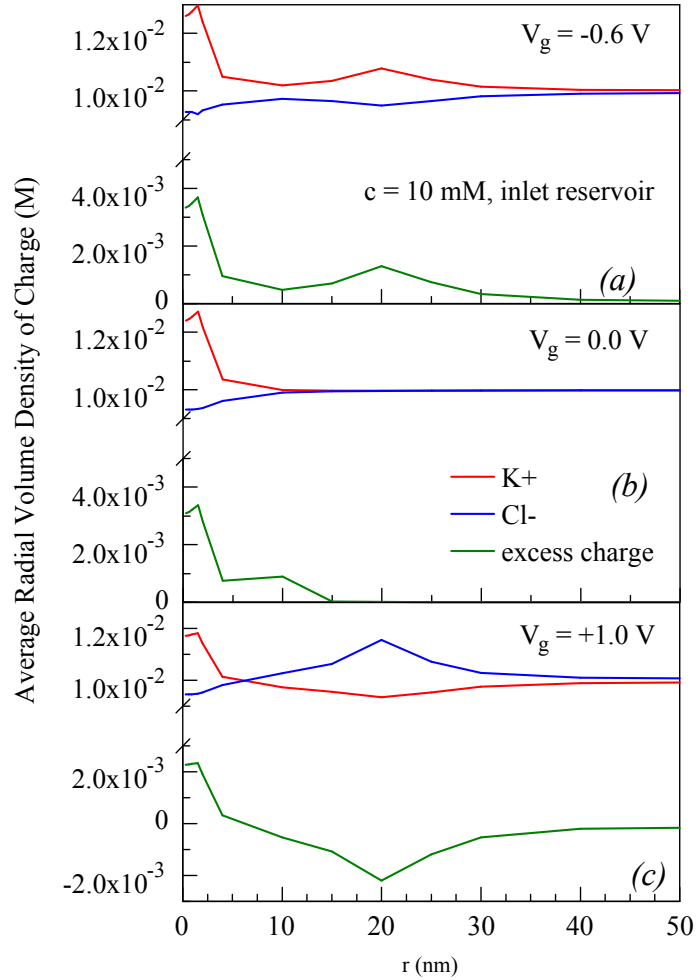


Figure S15. Radial distribution of the charged particles and the excess charge in the inlet reservoir, averaged over the axial length of the reservoir.

The velocity field and streamlines of the fluid, shown in Figure S17(a), illustrate the electroosmotic current (of velocity v) close to the slip internal surfaces of CNT, as obtained from the Stokes equation (S3). The total flux streamlines of the charged particles, which is conserved in going from source to the drain reservoir, through the nanotube, is shown in Figure S17b. The conservation of the total flux of the charged particles (conservation of the total current) which follows from the Nernst-Planck equation (S2) is achieved with at least 3-digits accuracy in all cases.

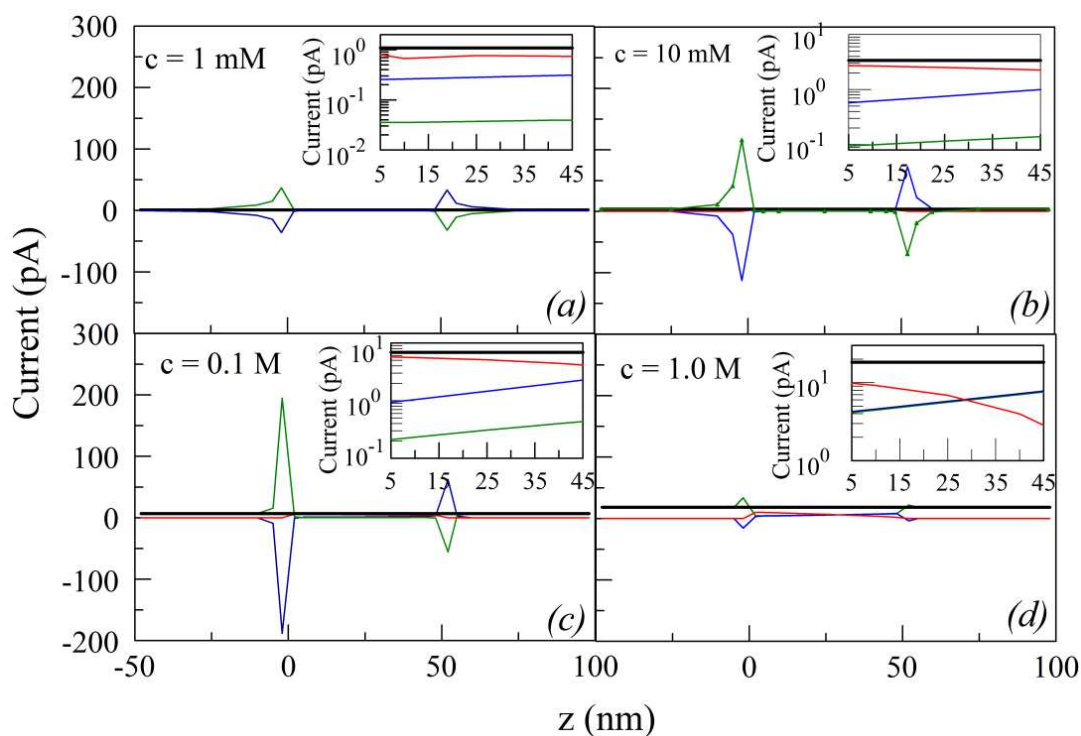


Figure S16. The various components of the total electric current (integrated over the relevant cross-sectional surfaces orthogonal to z , at various concentrations and at $V_g=0$: Total current (black), electroosmotic (red), diffusion (blue) and electrophoretic (green).

The electric field streamlines as well as the equipotential lines of the whole considered system are shown in Figure S18 for the case of $V_g=-0.6$ and $c=10$ mM. The surface charge at the border of the fluid and SiO_2 is calculated from the difference of the electric displacements at both sides of the surfaces and is negligible. The surface charge density is largest at the ends of the CNT, which is partially responsible for a large accumulation of charge at the CNT mouths.

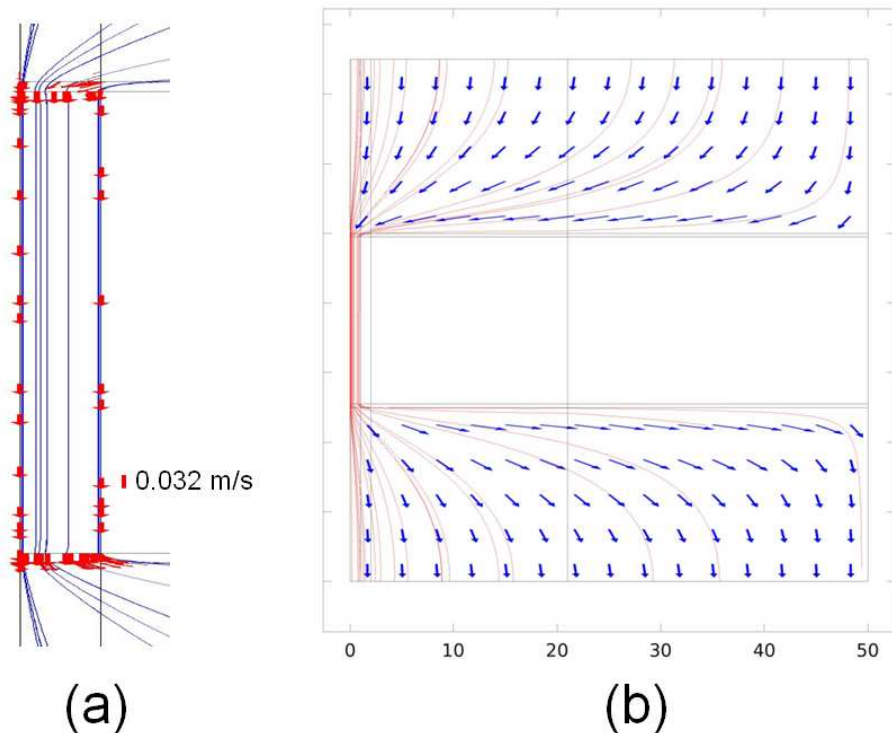


Figure S17. (a) Velocity stream lines and velocity vectors (arrows) for $c = 10$ mM and $V_g = -0.6$ V. **(b)** The electric flux streamlines for $V_g = -0.6$ V and $c = 10$ mM.

The far-field boundary conditions are applied at both fluid and SiO_2 boundaries at large r , resulting in zero normal component of the electric field close to these surfaces. The huge electric field of the gate electrode is mainly screened by the CNT surface and doesn't influence directly the field inside the CNT, but has a large influence at the ends of the tube, inducing charges at the tube mouths. Note that the radial electric field in the tube, is the dominant component of the field. The smallness of the axial component of the field explains relatively small value of the electroosmotic current for this short tube ($L = 50$ nm).

Arrow: Electric field Streamline: Electric field Contour: Electric potential (V)

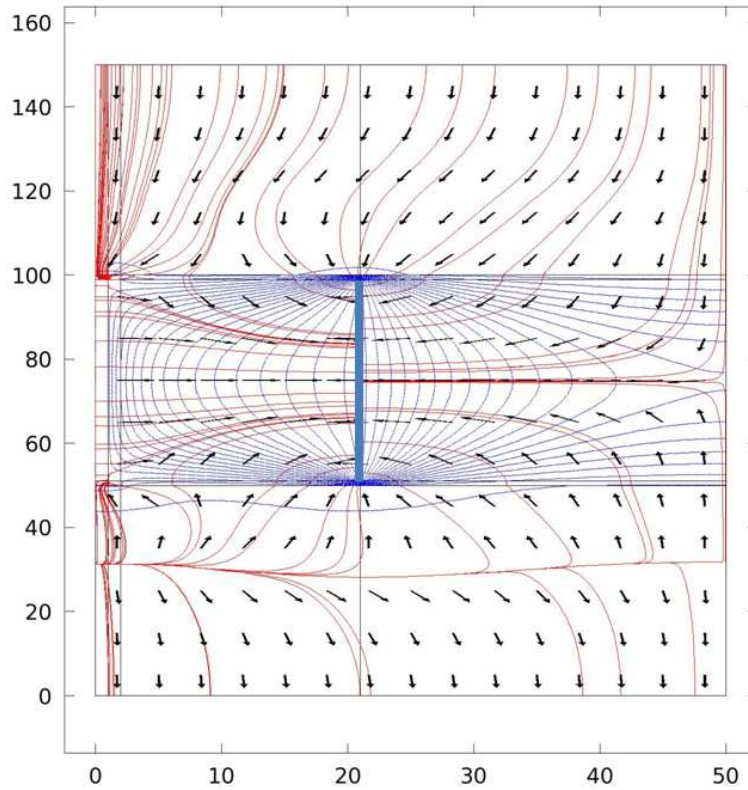


Figure S18. Electric field lines (red) and electric field vectors (arrows); Equipotential lines (blue) in the considered system, when gate potential is $V_g = -0.6$ V, and the total charge at the CNT surface is as in Table 1. The gate electrode is sketched by a blue thick line. The length of the electric field vectors is not proportional to its strength.

The axial variation of electric potential at $r=0.9$ nm, from the source electrode $z=-50$ nm), through the CNT (0-50 nm), to the drain electrode ($z=100$ nm) is shown in Figure S19. This potential mostly reflects the potential of the floating carbon nanotube surface for various concentrations and gate voltages, shown in Figure S20. The radial variation of the potential inside the tube is small, as shown in Figure S21.

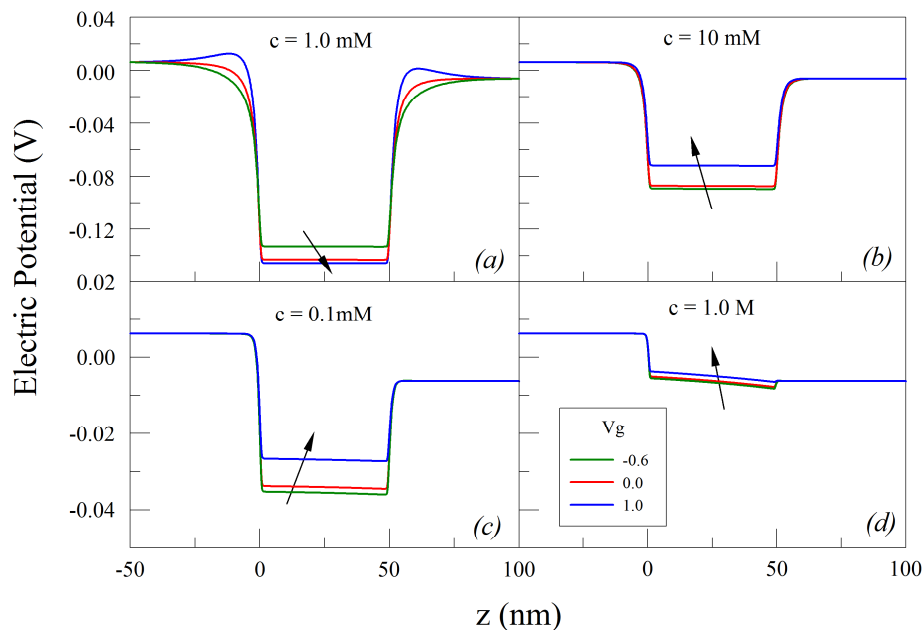


Figure S19. Axial distributions of the electric potential at $r=0.9$ nm, for various KCl concentrations c and various gate potentials V_g .

Due to the tube screening, the response of the potential inside the tube to variations in V_g is small, though it is biggest for $c=10$ mM, which agrees with the measured highest sensitivity to the gate potential at this concentration.

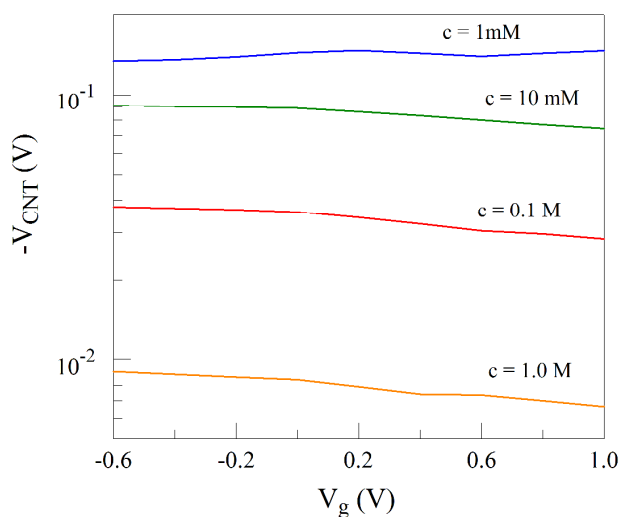


Figure S20. Potential of the floating CNT for various gate voltages, at $V_0=0.0125$ V.

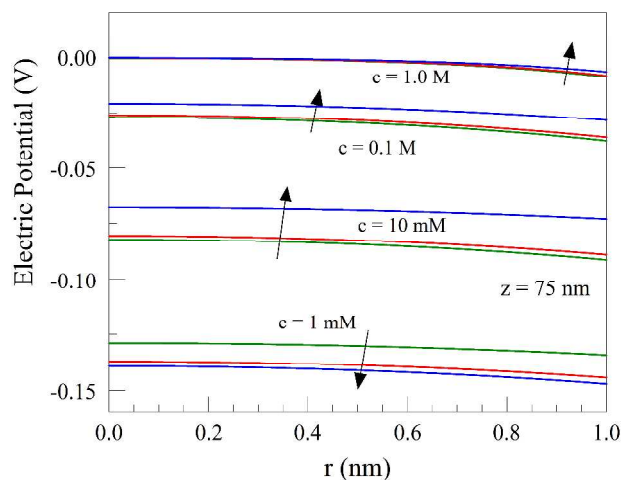


Figure S21. Radial distributions at the middle of the tube for the cases in Figure S20.

Finally, in Figure S22 we show the axial variation of the electric field in the system, at $r=0.9$ nm (close to the internal wall of the tube). Compatible with a sudden change of potential at the mouths of the CNT in Figure S19, two peaks of the electric field of opposite signs and approximately same heights are visible at the tube entrances. One of these peaks drives particle of positive charge sign, the other one is opposing the motion of the same particles.

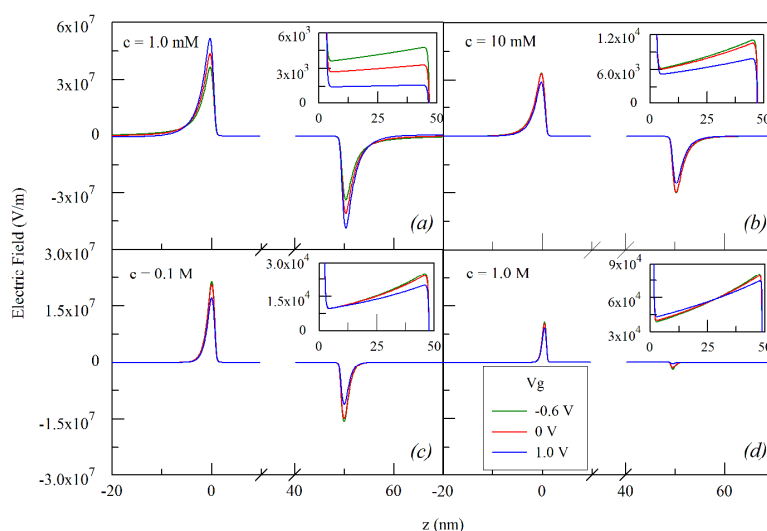


Figure S22. Axial distribution of the z -component of electric field, for various concentrations of KCl, at $r=0.9$ nm. Insets show the electric field inside the CNT as functions of the gate voltage V_g .

These peaks are responsible for the large components of the electrophoretic current in Figure S17 at the entrances of the tube. Large accumulation of the charges at the CNT entrances, on the other hand, is responsible for the large diffusion current peaks at Figure S17, which cancels the electrophoretic components. Thus, the current in the tube, dominated by the electroosmotic component, is controlled by the relatively small values of the axial field inside the tube, shown in the insets of Figure S22. The dependence of this field on the gate voltage is a function of concentration of KCl. For lower concentrations, it increases when V_g changes from -0.6 to 1 V, which competes with the opposite trend of the volume charge inside the tube for the magnitude of electroosmotic current. Namely, the electroosmotic current is proportional to the product of the fluid velocity and excess charge, where the velocity is proportional to the electric field in the tube. We also note that with increase of the KCl concentration, the peaks of the field at the tube entrances are increasingly asymmetric, with the positive field peak dominating at the source side of the tube. As a consequence, the asymmetry of the field at entrances has a role of a pump for positive ions, increasing diffusive and electrophoretic components of the currents in Figure S17, and certainly contributing to the increase of the conductance of the system in Figure S11a.

7.7 Slip length of a charged SWCNT

In order to connect the atomistic results (MD) which were run without any assumptions about the slip length, and the continuum dynamics which uses slip length to define the boundary condition of slipping at the CNT wall we perform the following analysis:

The Stokes' equation for cylindrical tube without the pressure gradient is

$$\mu \frac{d^2 u}{dr^2} = n E_{ext} \quad (S6)$$

where u is the axial velocity, n is the excess charge, and E_{ext} is the external electric field. From the azimuthal symmetry of the problem, it follows that $r=0$ is a stationary point, i.e.

$$du/dr(r=0) = 0 \quad (S7)$$

The definition of slip velocity, i.e. the tangential fluid velocity at the wall, u_{wall} ,

$$u_{wall} = L_s \left(\frac{du}{dr} \right)_{r=R} \quad (S8)$$

where L_s is slip length, and obviously

$$u(r=R) = u_{wall} \quad (S9)$$

The general solution of equation (S6) can be expressed in a simple form

$$u(r) = \frac{A}{2} r^2 + Br + C \quad (S10)$$

where A, B, and C are constant, and B = 0 from equation (S7), while from equation (S6)

it follows $A = \frac{nE_{ext}}{\mu}$, and then from equations (S6-S9)

$$C = -\frac{A}{2} R^2 + ARL_s \quad (S11)$$

Combining equations (S10) and (S11) yields

$$u(r) = \left(\frac{nE_{ext}}{\mu} \right) \left[\frac{r^2 - R^2}{2} + RL_s \right] \quad (S12)$$

The mean velocity over the radius is defined as

$$u_{mean} = \frac{\int_0^R u(r)(2r)dr}{R^2} = R \left(\frac{nE_{ext}}{\mu} \right) \left(L_s - \frac{1}{4} R \right) \quad (S13)$$

On the other hand, we calculate the mean velocity by the molecular dynamics calculations, and then equation (S13) gives the slip length L_s . Thus, once we have the mean velocity from molecular dynamics simulation, the slip length can be obtained provided R (radius of nanotube), n (excess charge), E_{ext} (external electric field), and μ (medium viscosity) are given.

The slip lengths were computed for (16,16) CNT, with its outer diameter being 2.5096 nm and inner diameter being 1.8296 nm and with a center-to-center diameter of

2.1696 nm (SI of Ref. 1). The electric field for molecular dynamics simulation is 2 V/μm. Such a large field is required for numerical stability, smaller fields leading to a large uncertainty in results. To compute the axial velocity for the smaller electric field, it could be scaled down with the applied electric field¹. The computed velocities are roughly in agreement with the data from Ref. 1, when the same conditions are used. The sampling size in the present calculation is 30,000.

Tables S4 and S5 show slip lengths and mean fluid velocities as a function of surface charge, for excess cation charge of $n=0.89$ M and $n=1.82$ M, respectively. Note that the calculation in MD is here done for an infinite, z-periodic CNT, with axial period of 10 nm. Coulomb cutoff is 4.9 nm (radius).

$n = 0.89$ M, $E_{\text{ext}} = 2$ V/μm			
Surface charge density (C/m ²)	0.0	-0.02	-0.05
Mean velocity (m/s)	7.2	5.4	3.0
Slip length (nm)	37.3	30.0	15.5

Table S4. slip length as a function of surface charge for $n = 0.89$ M, $E_{\text{ext}} = 2$ V/μm

$n = 1.82$ M, $E_{\text{ext}} = 2$ V/μm				
Surface charge density (C/m ²)	0.0	-0.01	-0.02	-0.05
Mean velocity (m/s)	14.1	8.7	6.5	6.0
Slip length (nm)	36.0	22.2	16.6	15.3

Table S5. slip length as a function of surface charge for $n = 1.82$ M, $E_{\text{ext}} = 2$ V/μm

We stress that the slip lengths were computed from the procedure described above, using the mean velocities from the molecular dynamics simulations, and are also shown graphically as functions of the surface charge density in Figure S23.

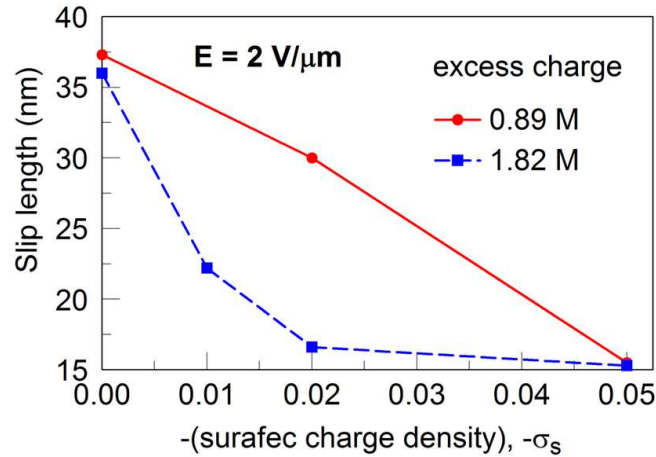


Figure S23. Calculates slip length at the CNT inner wall as function of the homogeneous CNT surface charge density for two concentrations of KCl

As can be seen in the Figure S23, the slip length slowly decreases with increase of the negative surface charge density, and stays large in comparison to the CNT diameter, for the considered range of the surface charges. Note that the total charge of $37.5e$ on the 50 nm CNT corresponds to the 0.02 C/m^2 charge density. If charges are varied with V_g to fit experimental values of conductance, that would change the charge density by at most $\pm 0.01 \text{ C/m}^2$. Here considered range is wider. Our results are consistent with the observation by Huang et al.¹³ The slip length of 37 nm (in absence of surface charge) is in good agreement with the experimental value of 33 nm.^{14, 15} We note that in the electrolyte the number of ions is much smaller than that of water molecules (less than 4% for 2M).

Although the real slip length is finite, it is an order of magnitude larger than the diameter of CNT (2 nm), so the perfect slip boundary conditions on the CNT surface, assumed in our calculations, are a reasonable choice, which are not expected to introduce any significant error in the results.

7.8 Velocities and mobilities

Electroosmotic velocities (Figure S24) for our model system, averaged over the cross section of the tube at the middle of its length, were calculated from coupled PNPS equations, follow specifically from Stokes equation (S3). Radius-averaged electroosmotic mobilities (Figure S25) are calculated from by radial averaging at the middle of the tube length ($L = 50 \text{ nm}$) of $\mu_{eo} = U_{eo}/E$, where E is the axial electric field inside the tube, obtained specifically from the Poisson equation (S1). The electrophoretic velocity of ions (here, anions K^+) is relative to the solvent, and is calculated from definition of mobility, i.e. $v_{ep} = \mu_{ep}E$, where μ_{ep} is taken to be the average bulk mobility of a particular ion (this is, therefore an input into equations). In Figure S24 we use mobility of K^+ ions ($7.62 \times 10^{-8} \text{ m}^2/\text{Vs}$). Note that the ratio of averaged electroosmotic to electrophoretic velocities is about 20 for 1 mM (at $V_g = 0$), slightly decreases with concentration, and doesn't depend significantly on V_g . Also, the ratio of electroosmotic and electrophoretic currents is proportional to the respective velocity ratio, and is increasing with the SWCNT length (See Figure S10). Thus, Figure S10 shows various components of electric current through

the CNT for $V_g=1$ V, KCl concentration of 1 M, and $V_{sd}=0.05$ V, for the tube lengths of (a) $L=200$ nm, with $Q=-6 \times 10^{-17}$ C $=-369e$, and (b) $L=500$ nm, $Q=-4 \times 10^{-16}$ C $=-2500e$. The ratio of electroosmotic current (red line) to electrophoretic current in S10 is 234:1 for $L = 200$ nm and 3943:1 for $L = 500$ nm (3 nm rounded ends of the tubes are not shown)

We note that the calculated current has three components: the diffusion, electrophoretic, and electroosmotic. The ion migration velocity (relative to the solvent) is sum of electrophoretic and diffusion components. Since the diffusion component in our consideration is not negligible in comparison to the electrophoretic one (see Figure S16 for the relevant current components), electrophoretic velocity cannot be calculated simply as the difference of the total ionic and electroosmotic velocities.

When compare these electroosmotic velocities with those obtained by MD (or in the Ref. 1), the electroosmotic velocities obtained here show much smaller values. The reason is simple: The current here corresponds to a much smaller electric field. In case of MD the electric field is calculated (for the length period of 10 nm) assuming it is homogeneous along the infinite tube. However, in the continuum calculations, solution of coupled PNPS equations gives the accurate values of the electric field, showing that the most of the voltage drop along the tube is localized at its mouth (see Figures S19 and S22), while the fields in the middle of the tube are smaller by about 100 times from those used in MD, leading to proportionally smaller electroosmotic velocities, and smaller ratios of electroosmotic to electrophoretic velocities.

The radial variation of the electroosmotic velocity, for various concentrations of the electrolyte and various gate voltages V_g is very small, reflecting the typical electroosmotic profile with large slip length.

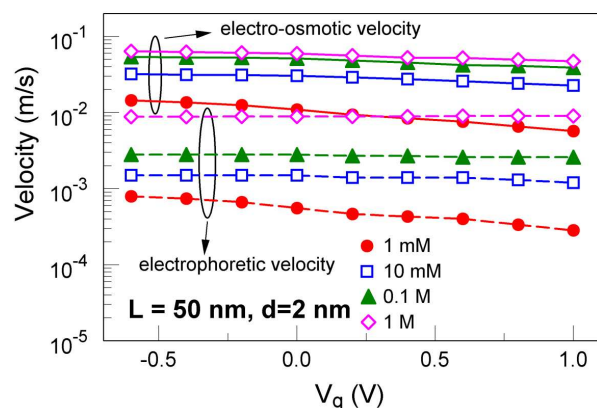


Figure S24. Axial electroosmotic and electrophoretic velocities for various ion concentrations.

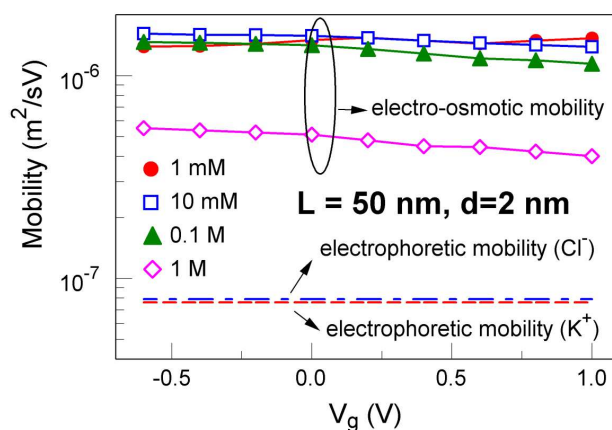


Figure S25. Electroosmotic and electrophoretic mobilities for various ion concentrations.

To get an idea how of the mobilities are changing with the CNT length, we compare the relevant quantities for lengths of $L=50$ and 200 nm, varying the KCl concentrations, as well as of $L=500$ nm (for one case, $c=1M$). Since the mobilities are varying along the tube, we present values averaged over both radius and the tube length (not counting the mouth regions).

concentration	Velocity (m/s)	Electric Field (V/m)	EO mobility (m^2/Vs)
1mM	9.4×10^{-3}	7.8×10^3	1.2×10^{-6}
10 mM	3.2×10^{-2}	2.3×10^4	1.4×10^{-6}
0.1 M	5.4×10^{-2}	4.5×10^4	1.2×10^{-6}
1 M	6.2×10^{-2}	1.3×10^5	4.8×10^{-7}

Table S6. Velocity, electric field, and electroosmotic (EO) mobility for various concentrations with $L=50$ nm, $Q=-37.5e$.

concentration	Velocity (m/s)	Electric Field (V/m)	EO mobility (m ² /Vs)
1mM	0.039	3.6×10^3	1.1×10^{-5}
10 mM	0.16	1.4×10^4	1.15×10^{-5}
0.1 M	0.35	3.2×10^4	1.0×10^{-5}
0.2 M	0.36	4.3×10^4	8.5×10^{-6}
1 M	0.17	1.2×10^5	1.4×10^{-6}

Table S7. Velocity, electric field, and electroosmotic (EO) mobility for various concentrations with L=200 nm, Q=-312.5e.

concentration	Velocity (m/s)	Electric Field (V/m)	EO mobility (m ² /Vs)
1 M	2.82	32906	8.5×10^{-5}

Table S8. Velocity, electric field, and electroosmotic (EO) mobility for various concentrations with L=500 nm, Q=-3750e.

Averaged cationic mobilities for various tube lengths and KCL concentrations are shown in Figure S26. The EO mobilities are increasing with the SWCNT length. The conclusions in this subsection require more various-length calculations to offer final quantitative estimates of the length effects.

Considering the SWCNT diameter uncertainties in experiment, we have also calculated the electroosmotic velocities as functions of the SWCNT external diameter by MD in Ref. 1. Comparing with the value of 1.7nm diameter SWCNT, the electroosmotic velocities (same for mobilities) are reduced to 36% and 27% for 2.5nm and 3nm SWCNT respectively, indicating that the role of electroosmotic current decreases with increase of the CNT diameter.

Finally, let's put the calculated EO mobilities in context with recent experimental results. Wu *et al.* reported an electroosmotic velocity of 4.8×10^{-4} m/s (at -0.3V) using ensemble of MWCNTs(7nm inner diameter) and the flux was measured by UV-Vis.¹⁶ The mobilities is roughly 8×10^{-9} m²/Vs (assuming the CNT is 5μm long) from the velocity. The inner surface of the CNT was modified with negatively charged molecules and the increased surface charge density leads to the enhanced electroosmotic velocity of cationic and neutral molecules. Strano's group¹⁷ studied the ionic transport through one or a few very long SWCNT (500μm) with average diameter of 1.5nm. Spikes were observed in

ionic current and were attributed to single ion blockage events. They reported an enhanced mobility of potassium ions ($\sim 8 \times 10^{-6} \text{ m}^2/\text{Vs}$ or a velocity of $8 \times 10^{-3} \text{ m/s}$ at 0.5 V), using the spike width and CNT length.

As shown in our calculations, the electroosmotic mobility is about $1 \times 10^{-5} \text{ m}^2/\text{Vs}$ for a model system with length 200 nm and diameter 2 nm ($c < 0.1 \text{ M}$). This mobility value is close to Strano's experiments (assuming electroosmosis dominates) but about 3 orders of magnitude higher than the large MWCNTs. The very long CVD grown SWCNT normally have fewer defects along the tube. More importantly, the SWCNT may contain a much higher surface charge due to the device geometry. The single layer carbon wall also cannot effectively screen out the nearby environmental charges. That is also the reason we can use gate electrode to effectively modulate the ionic flow.

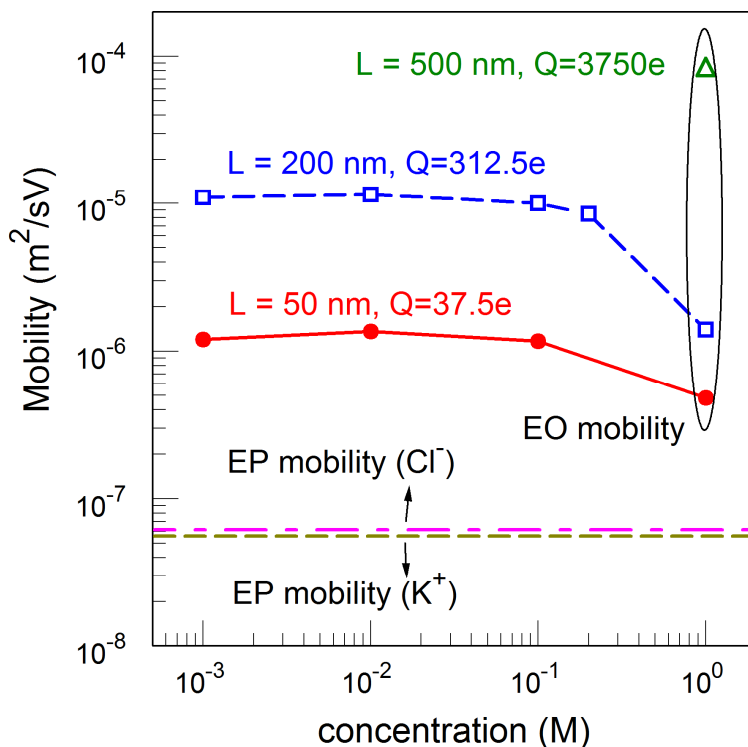


Figure S26 Averaged electroosmotic mobilities for the K^+ as functions of the KCl concentrations, for various CNT lengths.

References:

1. Liu, H.; He, J.; Tang, J.; Liu, H.; Pang, P.; Cao, D.; Krstic, P.; Joseph, S.; Lindsay, S.; Nuckolls, C., Translocation of Single-Stranded DNA Through Single-Walled Carbon Nanotubes. *Science* 2010, 327, 64-67.
2. Li, Y.; Kim, W.; Zhang, Y.; Rolandi, M.; Wang, D.; Dai, H., Growth of Single-Walled Carbon Nanotubes from Discrete Catalytic Nanoparticles of Various Sizes. *J. Phys. Chem. B* 2001, 105, 11424-11431.
3. Majumder, M.; Chopra, N.; Hinds, B. J., Mass Transport through Carbon Nanotube Membranes in Three Different Regimes: Ionic Diffusion and Gas and Liquid Flow. *ACS Nano* 2011, 5, 3867-3877.
4. Javey, A.; Shim, M.; Dai, H., Electrical Properties and Devices of Large-Diameter Single-Walled Carbon Nanotubes. *Appl. Phys. Lett.* 2002, 80, 1064.
5. Kirby, B. J., *Micro- and Nanoscale Fluid Mechanics*. Cambridge University Press: New York: 2010.
6. Pivonka P.; Smith, D., Investigation of Nanoscale Electrohydrodynamic Transport Phenomena in Charged Porous Materials. . *Int. J. Numer. Meth. Engng.* 2005, 63, 1975-1990.
7. Szymczyk, A.; Zhu, H.; Balannec, B. a., Pressure-Driven Ionic Transport through Nanochannels with Inhomogenous Charge Distributions. *Langmuir* 2010, 26, 1214-1220.
8. Daiguji, H.; Yang, P.; Majumdar, A., Ion Transport in Nanofluidic Channels. *Nano Lett.* 2004, 4, 137-142.
9. Joseph, S.; Aluru, N. R., Why Are Carbon Nanotubes Fast Transporters of Water? *Nano Lett.* 2008, 8, 452-458.
10. Kar, S.; Vijayaraghavan, A.; Soldano, C.; Talapatra, S.; Vajtai, R.; Nalamasu, O.; Ajayan, P. M., Quantitative Analysis of Hysteresis in Carbon Nanotube Field-Effect Devices. *Appl. Phys. Lett.* 2006, 89, 132118.
11. COMSOL Multiphysics Quick Start and Quick Reference, COMSOL AB. <http://www.comsol.com>.
12. <http://graa.ens-lyon.fr/MUMPS/>.

13. Huang, D. M.; Cottin-Bizonne, C.; Ybert, C.; Bocquet, L., Aqueous Electrolytes near Hydrophobic Surfaces: Dynamic Effects of Ion Specificity and Hydrodynamic Slip†. *Langmuir* 2008, 24, 1442-1450.
14. Holt, J. K.; Park, H. G.; Wang, Y.; Stadermann, M.; Artyukhin, A. B.; Grigoropoulos, C. P.; Noy, A.; Bakajin, O., Fast Mass Transport Through Sub-2-Nanometer Carbon Nanotubes. *Science* 2006, 312, 1034-1037.
15. Majumder, M.; Chopra, N.; Andrews, R.; Hinds, B. J., Nanoscale Hydrodynamics: Enhanced Flow in Carbon Nanotubes. *Nature* 2005, 438, 44-44.
16. Wu, J.; Gerstandt, K.; Majumder, M.; Zhan, X.; Hinds, B. J., Highly Efficient Electroosmotic Flow Through Functionalized Carbon Nanotube Membranes. *Nanoscale* 2011, 3, 3321-3328.
17. Lee, C. Y.; Choi, W.; Han, J. H.; Strano, M. S., Coherence Resonance in a Single-Walled Carbon Nanotube Ion Channel. *Science* 2010, 329, 1320-1324.